J Mater Sci (2010) 45:2157–2164
DOI 10.1007/s10853-009-3982-x

HTC2009

Observed behavior of various oxide inclusions in front of a solidifying low-carbon steel shell

Kristofer J. Malmberg · Hiroyuki Shibata · Shin-ya Kitamura · Pär G. Jönsson · Seiji Nabeshima · Yasuo Kishimoto

Received: 15 June 2009 / Accepted: 12 October 2009 / Published online: 30 October 2009

Abstract The engulfment and pushing (extrusion) of inclusions during solidification play an important role in the formation of a steel structure and, as a result, for the mechanical properties of the final steel product. The aim of this study is to gain knowledge about the behavior of non-metallic inclusions at the interface between a growing solid front and a liquid phase. The focus is on the effect of the titanium and titanium oxide content on the inclusions and the different phenomena, which occurs at the solid/liquid interface. This was studied in samples of low-carbon steels de-oxidized by different combinations of Al, Ca, and Ti. For this purpose, each metal sample of 0.19 g was melted at a temperature close to 1550 °C in an argon atmosphere and solidified under different solidification rates. A direct observation of inclusion behavior during solidification was made using a confocal scanning laser microscope equipped with an infrared gold image furnace. The alloying elements in the sample varied between: C 0.002–0.044; Si 0.02–1.33; Mn 0.12–1.33; P 0.003–0.016; S 0.003–0.01; Al 0.002–0,033; Ni 0–0.28; Cr 0–0.25; Ti 0.008–0.065; Ca 0.0007–0.002; O 0.002–0.0114 and N 0.0028–0.0056 (mass%). Several types of inclusions with different morphologies were found within the sample. The morphology of the observed inclusions on the molten steel surface varied from round alumina and calcium-oxide-rich inclusion to needle-shaped titanium oxide-rich inclusions. The observed motions of the inclusions at the vicinity of the front of the solidifying steels were classified. At a low solidifying velocity and a small inclusion size, inclusions flowed away from the solidifying front. Furthermore, they also or got pushed a distance and thereafter flowed away from the interface. At a medium velocity and a slightly bigger size, inclusions tend to get pushed in front of the solidifying front. Another observation was that at a high velocity and a large particle size, inclusions tend to get engulfed or pushed and then engulfed by the progressing front. The relationship among the morphology, chemical composition of inclusions and the solidifying velocity is discussed in this article.

K. J. Malmberg (✉) · H. Shibata · S. Kitamura
Institute of Multidisciplinary for Advanced Materials, Tohoku University, 2-1-1 Katahira Aobaku, Sendai 980-8577, Japan
e-mail: kmal@b.kth.se

H. Shibata
e-mail: shibata@tagen.tohoku.ac.jp

K. J. Malmberg · P. G. Jönsson
Department of Materials Science and Engineering, Royal Institute of Technology (KTH), 100 44 Stockholm, Sweden

S. Nabeshima · Y. Kishimoto
Steel Research Laboratory, JFE Steel Corp, 1 Mizushima Kawasakidori, Kurashiki 712-8511, Japan

Introduction

Today, inclusion behavior at solid/liquid (hereafter S/L) interfaces represents a well-studied subject. However, it is still an important subject to steel industry with respect to cleanness and segregation in the final steel products. It is known that the usage of Ti in the de-oxidation process of steel increases the clogging in the so-called submerged entry nozzle (SEN) during continuous casting of steels [1]. Also, Basu et al. [2] have investigated the formation of inclusions during de-oxidation with titanium. They found that with Ti de-oxidation, inclusions containing titanium oxide were formed. These promoted a large-scale melt freezing in the SEN, which led to that the SEN was eventually clogged. This production disturbance represents a big economical issue for steel producers.

Kikuchi et al. [3], reported that with the addition of Ti during de-oxidation, the final micro-structure and solidifying micro-structure may be positively changed. From the solidification aspect, there are a few phenomena connected with the S/L interface, including the more known pushing and engulfment of inclusions [4]. In addition, many mathematical [5–8], computed [9, 10], and physical [11] models have also been used previously to better understand these phenomena. Moreover, in situ experiments have been made to clarify the differences between solid and liquid inclusion behaviors [12], at the S/L interface. Liquid inclusions are liquid at the same or at a lowest temperature than the melting temperature of the steel. The liquid phase of these inclusions is insoluble in the steel and therefore looks spherical while observed in a CSLM. Furthermore, to determine the critical velocities [4] at which the inclusion gets engulfed by the S/L interface.

In this study, three different steel samples were investigated with the focus on the effect of the titanium content in the steel and the titanium oxide content in the inclusions on the inclusion behavior at the S/L interface. The inclusions observed were formed during the processing of the steel. The in situ experimental work has been carried out using a confocal scanning microscope (hereafter CSLM) with a gold image furnace to investigate the effect of Ti de-oxidation on the inclusion behavior at S/L interface of steel and the critical velocity.

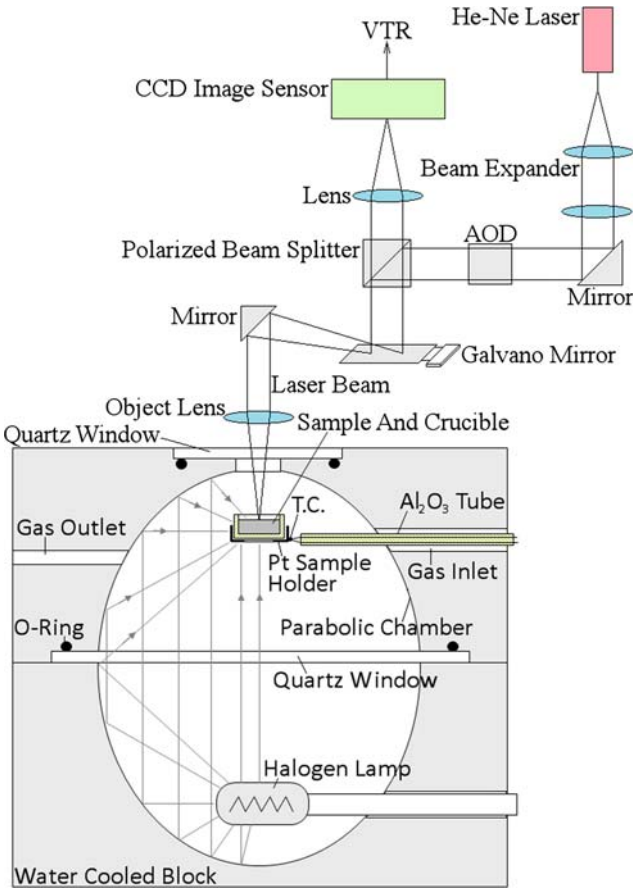

Fig. 1 Schematic picture of CSLM mounted together with an infrared image furnace

Experimental

Equipment

The experimental technique used in this study is a Confocal Scanning Laser Microscope (CSLM), using a He–Ne laser together with an infrared image furnace. The specifications of this microscope can be found elsewhere [12]. The infrared image furnace is directly mounted under the CSLM apparatus. Furthermore, the focus of the laser will hit a sample surface located inside the furnace, as seen in Fig. 1. The figure also shows a schematic diagram of the apparatus and its configuration. The infrared image furnace can suppress oxidation of the sample from the surrounding environment. During this study, the chamber was first evacuated from air and then placed under a constant flow of highly pure argon gas.

Experimental procedure

50 kg of pure iron was melted in an argon atmosphere in a high-frequency induction furnace. The temperature was kept at 1600–1620 °C. First, Al (0.002%) was added as pre-de-oxidation of the molten iron. Then, a Fe–Ti alloy was added and subsequently a CaSi alloy was added. After 8–10 min, the molten iron was cast into ingots with the dimensions 100 × 150 × H350 mm. Then samples were taken from positions 100 mm from the bottom and 20–25 mm from the surface of the cast sample. The obtained sample compositions are given in Table 1. The samples were ground and shaped into disks with a thickness of 2 mm and a diameter of 4.3 mm. Thereafter, these disks were placed in a high-purity aluminum oxide crucible with a 5.5-mm outer diameter and a 4.5-mm inner diameter. Then, they were placed inside the furnace and the furnace was turned on. At the start of the experiment, the sample was heated to 200 °C and kept for 20 min. The heating was done by increasing the power to the infrared

Table 1 The chemical composition of samples A, B, and C in mass percent

	C	S	Al	Ti	Ca	O
A	0.0110	0.010	0.002	0.065	0.0030	0.0053
B	0.0036	0.006	0.002	0.021	0.0016	0.0080
C	0.0052	0.007	0.002	0.008	0.0007	0.0114

lamp. This, in turn, resulted in an increased temperature inside the oven. At this stage, any unwanted moisture inside the furnace or on the sample was evaporated. Thereafter, the temperature of the furnace was increased to the melting temperature of the steel. More specifically, the temperature was initially increased by 100 °C/min. When the temperature of the furnace was close to the melting temperature of the steel, the heating of the furnace was manually controlled. Thereafter, when the sample started to melt, the temperature was slowly increased by controlling the power to the infrared lamp so that the S/L interface easily could be observed and kept under control. In addition, the temperature inside the furnace was slightly lowered to increase solidification velocity of the steel. The S/L interface movement and the behavior of the inclusions at the S/L interface were observed and recorded.

The recorded videos were carefully observed, and the fragments with interesting phenomena were cut out of the whole recording. The images were captured frame-by-frame with the interval of 1/30 s. These fragments were printed to measure the solidification velocity. In addition, the morphology of the inclusions was also measured from the printed frames.

Results and discussion

Engulfment, pushing, and flow of the inclusions in front of the S/L interface

Three different basic phenomena related to the motion of the inclusions were observed during the experiments: pushing, flow, and engulfment. In addition, two different combinations of these were also observed. The first of the three basic phenomena is well known and could be described as pushing [4] of an inclusion. This pushing phenomenon occurs when the solidification velocity of the steel is low enough to support pushing of the inclusion. Pushing means that the inclusion is forced to move in front of the progressing S/L interface. The second observed phenomenon was flow of the inclusions. When the solidifying interface progresses into the melt, the inclusion located at the interface flows away from the interface. This phenomenon has previously been studied by Nakajima et al. [13]. The mechanisms of this phenomena is not yet known, but one factor causing this behavior might be marangoni flow, caused by concentration differences in the melt.

The third phenomenon is the so called engulfment of the inclusions [4]. This phenomenon occurs when the solidification velocity is too high to support the pushing of the inclusion. What happens is that the inclusion gets stuck in the solid interface while the steel is solidifying. This occurs when the velocity of the interface reaches a so-called critical velocity. This velocity is reached when a certain inclusion with a specific morphology and composition gets engulfed.

Different combinations of these phenomena may also occur. One possible combination is that an inclusion is pushed by the progressing S/L interface. Thereafter, the solidification velocity increases due to a variation in temperature inside the furnace and the inclusion gets engulfed. However, when the same scenario occurs the solidification velocity decreases. This might lead to that then the particle may flow away from the solidifying interface. Overall, all the three phenomena discussed above were observed in all three samples. More specifically, they are illustrated in Fig. 2 in form of in situ CSLM observations. The three different phenomena are all the same scale and the photos have been captured at three different times during the observed inclusion behavior.

From Fig. 2 the phenomena of engulfment of the inclusions on the sample B can be observed from parts (a1) to (a3). At position a1, the inclusions shape was rectangular with the dimensions 9 μm × 4 μm. Furthermore, they were present at the front of the interface. Thereafter, the interface progressed from the righthand side of the figure to the lefthand side, where it engulfed the inclusion more to the part of (a2). At position (a3), the inclusion was almost completely engulfed at a critical velocity of 11 μm/s. The photos from (b1) to (b3) representing sample C show how spherical liquid inclusions with a diameter of roughly 4–7 μm flow away from the progressing interface. At (b1) the interface was not moving. However, in (b2) the interface starts to move from the lower side to the upper side at a velocity of 4.5 μm/s. Finally, at (b3) the inclusions flowed away from the interface. Finally, the photos (c1) to (c3) represent observations from sample B, in Fig. 2 the pushing of an inclusion is illustrated. The interface moved at a constant velocity of 7 μm/s from the righthand side to lefthand side in all the three photos. Also, the pushing of the inclusion, with a rectangular shape (8 μm × 3 μm) was cleary observed.

Chemical composition and morphology of the inclusions

The inclusion particles were observed by an Electron Probe Micro Analysis (EPMA) microscope to identify the chemical composition and morphology of the inclusions. Figure 3 shows photos taken of the sample surface that was observed at a high temperature with the CSLM microscope. It should be noted that the three different images are presented using a different scale. The image (a) shows the inclusion engulfed in Fig. 2. Image (b) is an overview photo of similar inclusions that showed the flow phenomena.

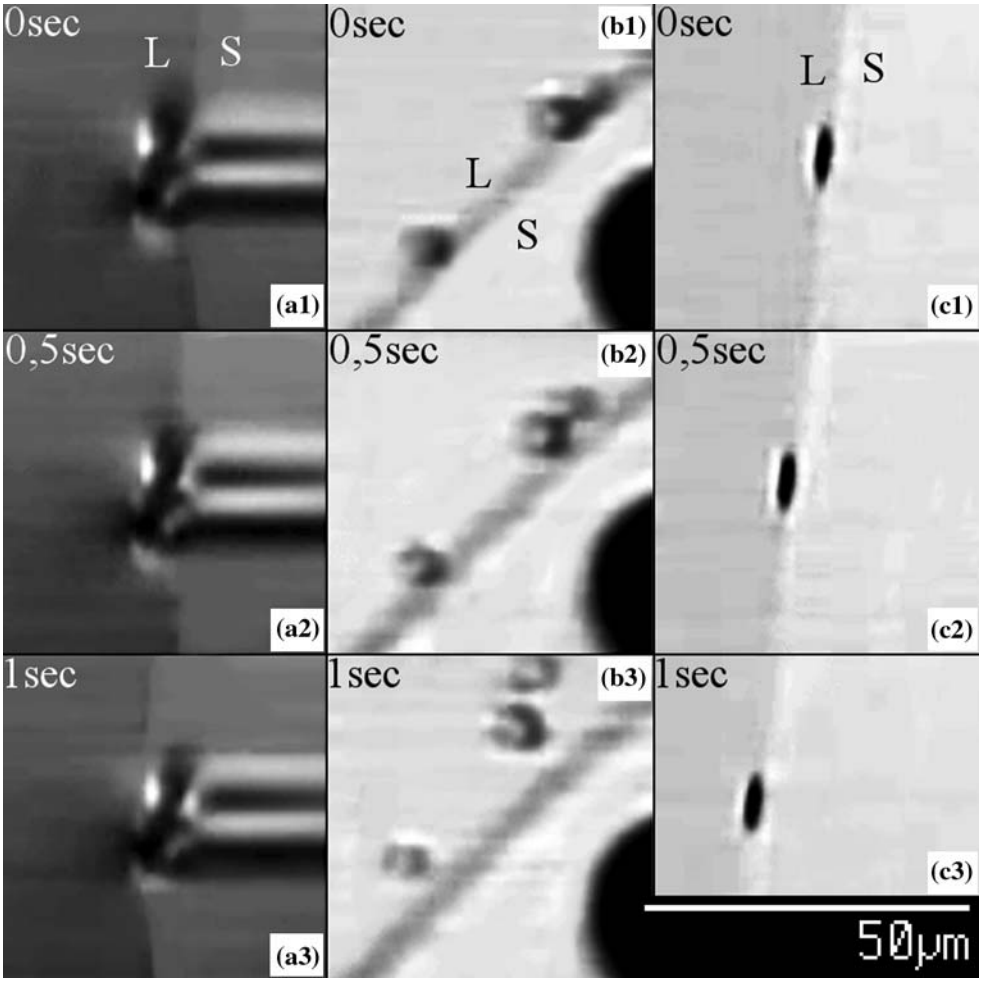

Fig. 2 Photos from the *left*: engulfment (**a1**–**a3**), flow (**b1**–**b3**), and pushing (**c1**–**c3**); *L* liquid, *S* solid

Furthermore, image (c) is the inclusion that showed the tendency of pushing.

Position (d) of Fig. 3 shows an inclusion containing a very high amount of titanium, which has a similar composition as the inclusions with a high titanium oxide content in Fig. 4a. Also, Table 2 shows the composition of the three different inclusions in terms of the contents of calcium oxide, aluminum oxide, and titanium oxide.

The relationship between the size, morphology, and chemical composition of the inclusions, and the velocity of the S/L interface in steel

The measured velocity of the S/L interface, the measured length of the inclusions with the observed morphology, and the TiO_X content of the inclusions are summarized in Fig. 4a and b for sample C, in Fig. 5a and b for sample B, and in Fig. 6 for sample A. In Fig. 4, the different phenomena are illustrated by the shape of the plots. The horizontal axis in Fig. 4 represents the length of the inclusions measured parallel to the S/L interface. Furthermore, this length represents the size of the inclusions in this study. In addition, a color or a dot in Fig. 4 shows the amount of TiO_X content inside the inclusion. Symbols with four different black shapes as illustrated in Fig. 4 symbolize a rough shape of the inclusions with different TiO_X composition ranges. Figure 4a and b shows the results for solid and liquid inclusions, respectively. This is due to that different critical velocities were observed for different states of the inclusions. The irregular shape of the symbol shows the irregular shape of the inclusions with a 75–80 mass% content of TiO_X in Fig. 4a. The rectangular shape of the symbol represents a rectangular shape of the inclusions with an 85–90 mass% content of TiO_X in Fig. 4a. The thin long shape represents the needle shape of the inclusions with an 88–96 mass% content of TiO_X in Fig. 4a. In Fig. 4b, the round shape of the symbol represents the round shape of the inclusions with a 17–20 mass% content of TiO_X, which were in liquid state at the observed temperatures.

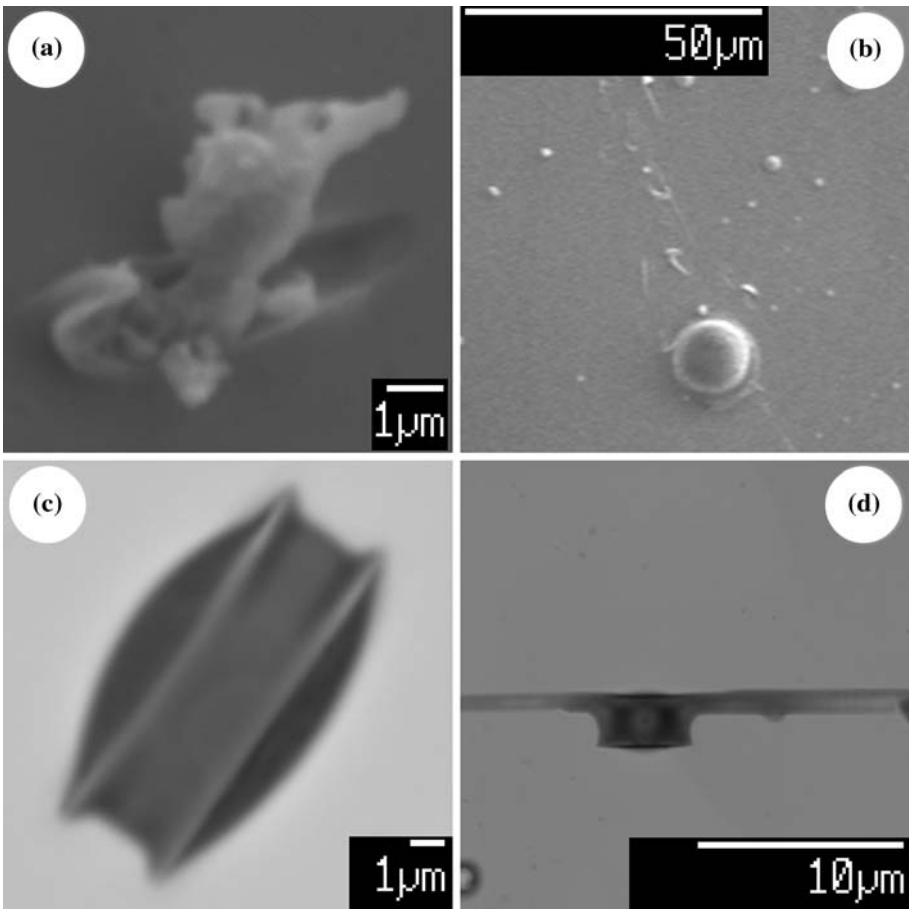

Fig. 3 Photos taken from the EPMA microscope. **a** An inclusion similar to the engulfed inclusion in **a** of Fig. 2, **b** similar inclusions as shown in Fig. 2 which illustrated the flow phenomena, **c** a similar inclusion getting pushed in Fig. 2, **d** a needle-shaped inclusion with a high TiO_X content

The solid lines show the estimated critical velocity of the S/L interface. As seen in Fig. 4, the dotted lines from previous study [12], represents a higher critical velocity than the results of this study for both the liquid and the solid cases. The critical velocities in Ref. [12] were given as a function of the inclusions radius. This was then re-calculated into an inclusion diameter, since the shape of many inclusions in this study could not be assumed to be round. For sample B, the critical velocities for both solid and liquid inclusions were also estimated as shown in Fig. 5.

From Fig. 7, one can observe three different inclusions. Figure 7a shows a liquid inclusion with its round shape that was observed in sample B. Figure 7b shows a semi-solid inclusion observed in sample A, where the center of the inclusion has a rough shape consisting of an outer soft (liquid) shell. Finally, Fig 7c shows a solid irregular-shaped inclusion observed in sample C. The critical velocity of sample A cannot be compared with the previous results of samples B and C, since the inclusions observed in sample A were in a semi-liquid state (Fig. 8).

In order to compare above-mentioned results with previous results, the solid lines with equations were compared with previous work from Shibata et al. [12], which are listed in Table 3. In previous work, the solid and liquid inclusions were found to be alumina and 30%CaO–30%SiO_2–40%Al_2O_3 inclusions, respectively. The critical velocity for liquid inclusions is lower than for solid inclusion, as previously shown by Shibata et al. [12]. The critical velocities varied among the three different samples A, B, and C. The critical velocities observed in sample B for the liquid and solid inclusions are slightly lower than those obtained in sample C; despite this, the chemical compositions of the inclusions for both samples B and C were similar for the solid and liquid inclusions. These results imply that the critical velocity is affected by the titanium content in the molten steel as well as by the TiO_X content in inclusions. For the inclusions which are semi-solid, as in sample A, the critical velocity is slightly higher than that for the inclusions containing TiO_X in the liquid state. Stefanescu and Catalina [14] derived theoretical equation to describe the critical velocity as follows:

$$V_{\mathrm{cr}} = \left(\frac{\Delta\gamma_0\, a_0^2}{3\eta k R}\right)^{1/2}. \tag{1}$$

To calculate $\Delta\gamma_0$, Eqs. 2 and/or 3 can be used.

$$\Delta\gamma_0 = \gamma_{\mathrm{PS}} - \gamma_{\mathrm{PL}} - \gamma_{\mathrm{SL}} \tag{2}$$

$$\Delta\gamma_0 = \gamma_{\mathrm{PS}} - \gamma_{\mathrm{PL}} \tag{3}$$

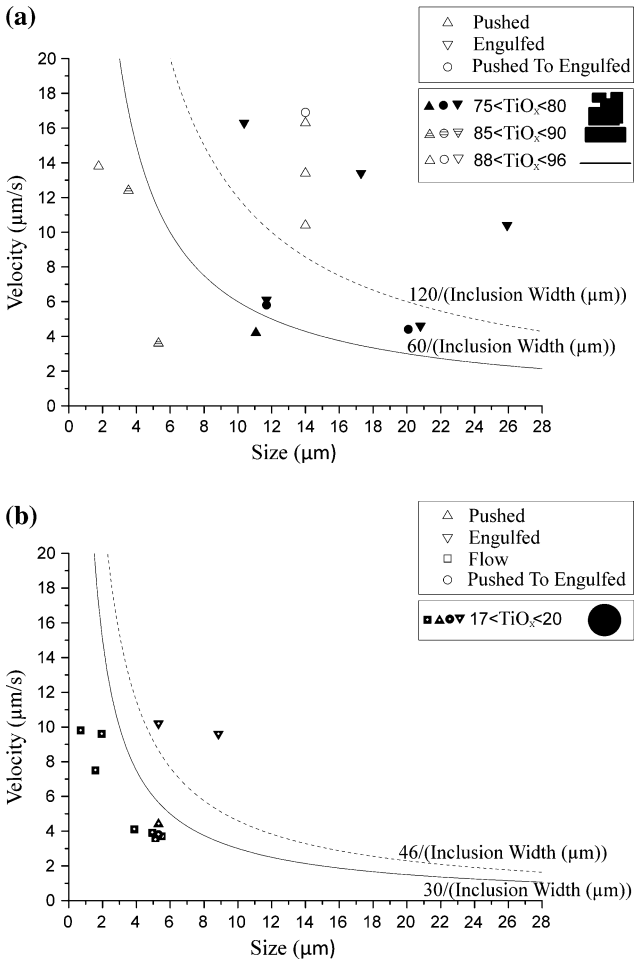

Fig. 4 The plots over sample C inclusion behavior with specific sizes and velocities. The size on the horizontal axis is the contact length of the inclusion, or in case of a spherical inclusion, the diameter. **a** High Ti content (solid inclusions), **b** low Ti content (liquid inclusions)

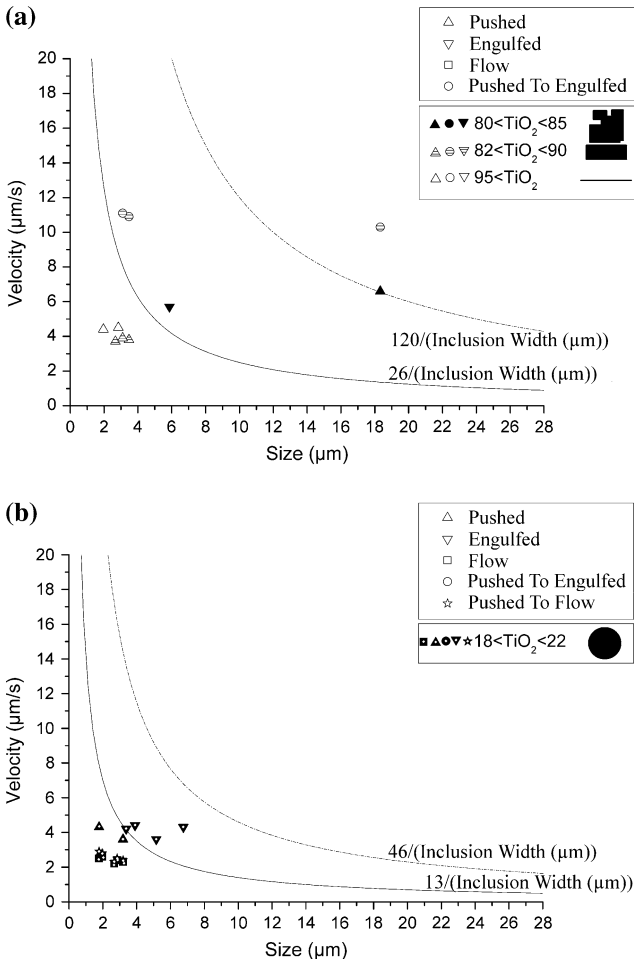

Fig. 5 The plots over sample B inclusion behavior with specific sizes and velocities. The size on the horizontal axis is the contact length of the inclusion, or in case of a spherical inclusion, the diameter. **a** High Ti content (solid inclusions), **b** low Ti content (liquid inclusions)

Table 2 The oxide compositions of the inclusions shown in Fig. 3 given in mass%

	a	b	c	d
CaO	0.6	30.7	0.6	0.1
Al_2O_3	9.3	42.3	3.4	1.6
TiO_x	90.1	27.96	96	98.3

where γ_{PS} is the interfacial energy between particle and solid steel, γ_{PL} is the interfacial energy between particle and molten steel, γ_{SL} is the interfacial energy between the solid and liquid metal, k is the ratio of k_p/k_L where k_p is the conductivity for the particle and k_L is the liquids conductivity, R is the particle radius, η is the viscosity of the molten steel, and a_0 is the atomic distance. However, due to the interest of thermodynamic calculations only Eq. 3 needs to be considered. Equation 2 can be used when kinetics need to be accounted for, as

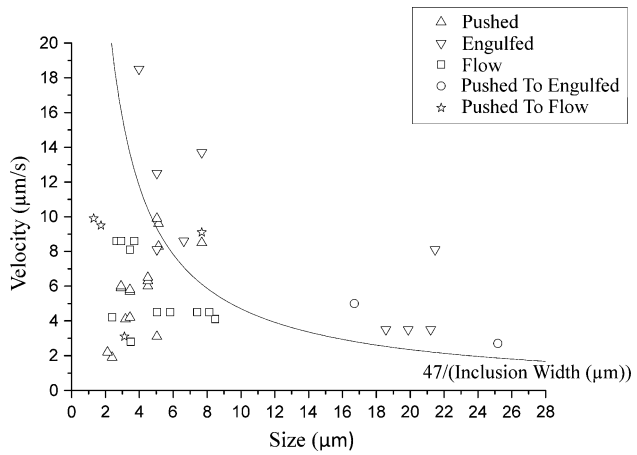

Fig. 6 The plot over sample A semi-solid inclusion behavior with specific sizes and velocities. The size on the horizontal axis is the contact length of the inclusion, or in case of a spherical inclusion, the diameter

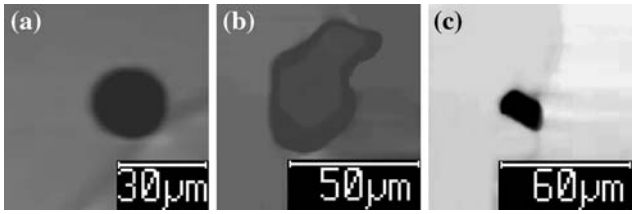

Fig. 7 **a** Completely round inclusion in liquid state observed in sample B, **b** semi-solid inclusion with solid parts in the middle and liquid parts in the periphery observed in sample A, **c** solid uneven-shaped inclusion

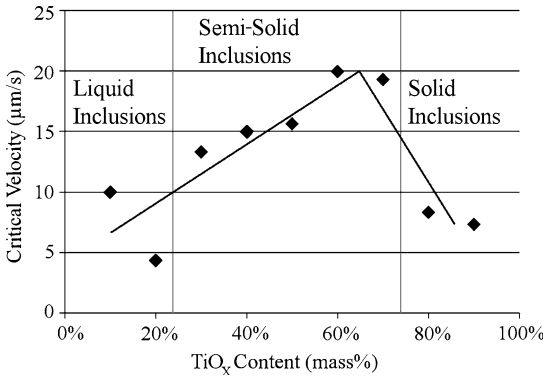

Fig. 8 The change of critical velocity with a change of the TiO_X content in the inclusion

Table 3 The different constants over the inclusion width (IW) (μm) for their critical velocities (μm/s) for samples A, B, and C

Sample	Equation	
A	Semi-solid inclusions	
	47 [IW (μm)]	
	21% $\langle Al_2O_3 \rangle$ 35%	
	11% $\langle CaO \rangle$ 29%	
	37% $\langle TiO_2 \rangle$ 64%	
B	Solid inclusions	Liquid inclusions
	25/[IW (μm)]	13/[IW (μm)]
	2% $\langle Al_2O_3 \rangle$ 14%	54% $\langle Al_2O_3 \rangle$ 70%
	0.5% $\langle CaO \rangle$ 5%	12% $\langle CaO \rangle$ 34%
	80% $\langle TiO_2 \rangle$ 98%	18% $\langle TiO_2 \rangle$22%
C	60/[IW (μm)]	30/[IW (μm)]
	8% $\langle Al_2O_3 \rangle$ 18%	44% $\langle Al_2O_3 \rangle$ 65%
	0.6% $\langle CaO \rangle$ 12%	24% $\langle CaO \rangle$ 36%
	75% $\langle TiO_2 \rangle$ 96%	17% $\langle TiO_2 \rangle$ 20%
Previous work [12]	120/[IW (μm)]	46/[IW (μm)]

However, since only semi-solid inclusions were found in sample A, only one equation could be calculated

described by Youssef et al. [15]. For samples B and C, the titanium content in sample B is higher than that in sample C. The resultant soluble oxygen content in sample B is lower than that in sample C. The interfacial energy between the observed inclusions and the molten steel was not available from our best knowledge. However, the interfacial tension data between Fe–O and Fe–Ti melts and alumina were summarized by Mukai et al. [16] as shown below.

For Fe–O melts as follows:

$$\gamma_{PL} = 1.320 - 0.777 \ln(1 + 40C_L). \quad (4)$$

For Fe–Ti melts as follows;

$$\gamma_{PL} = 1.029 - 0.612\, C_L. \quad (5)$$

where C_L is the soluble element content in the molten iron. In the case of inclusions containing TiO_X, the interfacial tension between molten iron and the inclusions is assumed to be of a similar magnitude as for alumina inclusions as expressed by Eqs. 4 and 5. To calculate the soluble element content, C_L, one can use Eq. 6 from [16].

$$C_L = C_0 \left[K_E + (1 - K_E)\, e^{\frac{-V_S(x-\delta)}{D_L}} \right] \quad (6)$$

where K_E is the effective distribution coefficient, V_S is the solidification velocity, x is the distance between the solidification interface and the inclusion, δ is the thickness of semi-solid layer between the solid at the liquid in the interface, and the D_L is the diffusion coefficient. To calculate C_L, one also needs to calculate the effective distribution coefficient, K_E, as follows:

$$K_E = \frac{K_0}{K_0 + (1 - K_0) e^{\frac{-V_S \delta}{D_L}}} \quad (7)$$

where K_0 (equilibrium distribution coefficient) is the C_S/C_L ratio, C_S is the fraction of the concentration of solid metal and C_L is the concentration of the liquid metal.

In Table 4, the values used for calculating γ_{PL} for samples B and C are given. Using these values and assuming that $\gamma^B_{PS} = \gamma^C_{PS}$, the values of $\Delta\gamma^B_0 = \gamma^B_{PS} - 1.007$ and $\Delta\gamma^C_0 = \gamma^C_{PS} - 1.024$ can be calculated. This, in turn, leads to the finding that $\Delta\gamma^B_0 > \Delta\gamma^C_0$. In addition, it also lead to the finding that $V^B_{cr} > V^C_{cr}$, which is the opposite results compared to the experimental results given in Table 3. However, with an addition of Ti into the steel, the oxygen content is also lowered, Thus, if the same calculations are carried out with the same assumption of $\gamma^B_{PS} = \gamma^C_{PS}$ the results show that $\Delta\gamma^B_0 = \gamma^B_{PS} - 1.10$ and $\Delta\gamma^C_0 = \gamma^C_{PS} - 1.02$. This leads to the finding that $\Delta\gamma^B_0 < \Delta\gamma^C_0$, which also means that $V^B_{cr} < V^C_{cr}$. These calculations correspond with the experimental results. From the calculated results, one can also see that the difference in $\Delta\gamma_0$ for samples B and C is bigger in the case of oxygen. This indicates that oxygen has a stronger effect on the critical velocity than titanium has.

Table 4 The values used for calculating the surface tensions for samples B and sample C

	δ (m) [16]	η (N*s/m^2) [16]	K_0 [16]	D_L (m^2/s) [16]	x (m) [16]	C_0^B [mass%]	C_0^C [mass%]	V_s (m/s)
Fe–O	10^{-5}	5×10^{-3}	0.02	2.6×10^{-9}	1×10^{-6}	0.008	0.0114	8×10^{-6}
Fe–Ti	10^{-5}	5×10^{-3}	0.40	4.5×10^{-9}	1×10^{-6}	0.021	0.008	8×10^{-6}

The values for C_0^B and C_0^C were taken from the sample composition and V_S was taken from the measured sample velocities

Conclusions

CSLM experiments with EPMA analysis were made of three steel samples that had been de-oxidized in different ways. The inclusion sizes, compositions, and the velocity of the solidifying interface were measured. An unexpected phenomenon, flow, was observed in all the three analyzed samples. The oxygen content in the steel is one of the governing factors that were found to control the critical velocity. More specifically, the inclusions containing a high amount of TiO_X were found to have a lower critical velocity than inclusions containing aluminum oxide. The experimental result showed that variations in the TiO_X content in the inclusions changes the critical velocity at which an inclusion gets engulfed. In addition, the increase of the titanium content in the steel can lead to a decreased oxygen content in the steel. This, in turn, may make the inclusions disperse in the steel product, since the critical velocity is lowered. Thus, a central segregation of inclusions can be suppressed.

Acknowledgement The authors would like to thank Dr. A. Karasev at the Royal Institute of Technology (Sweden) for fruitful discussions during preparation of this article.

References

1. Matsuura H, Wang C, Wen G, Sridhar S (2008) The transient evolution of inclusions in de-oxidized Fe–Ti–Al–O melts. In: Proceedings of international congress on the science a nd technology of steelmaking, Gifu, Japan, pp 424–427
2. Basu S, Choudhary SK, Girase NU (2004) ISIJ Int 44(10):1653
3. Kikuchi N, Nabeshima S, Kishimoto Y, Matsushita T, Sridhar S (2007) ISIJ Int 47(9):1255
4. Uhlmann DR, Chalmers B, Jackson KA (1964) J Appl Phys 35:2986
5. Ye Q-B, Li D-Q, Zhou D, Zhu Y-G (2007) Redistribution of insoluble particles during solidification. Sino-Swedish Structural Materials Symposium, pp 195–199
6. Hadji L (2002) Math Comp Model 36:147
7. Rempel AW, Worster MG (2001) J Cryst Growth 223:420
8. Ode M, Lee JS, Kim SG, Kim WT, Suzuki T (2000) ISIJ Int 40(2):153
9. Garvin JW, Yang Y, Udaykumar HS (2007) Int J Heat Mass Transf 50:2969
10. Garvin JW, Udaykumar HS (2003) J Cryst Growth 252:451
11. Ohta H, Suito H (2006) ISIJ Int 46(4):472
12. Shibata H, Yin H, Yoshinaga S, Emi T, Suzuki M (1998) ISIJ Int 38(2):149
13. Nakajima K, Yasuhiro S, Mizoguchi S, Imaishi N (2003) Met Mater Trans B 34B:37
14. Stefanescu DM, Catalina AV (1998) ISIJ Int 38:503
15. Youssef YM, Dashwood RJ, Lee PD (2005) Composites A 36:747
16. Mukai K, Lin W (1994) Tetsu-to-Hagané 80:533